The Astrophysical Journal, 765:45 (11pp), 2013 March 1 doi:10.1088/0004-637X/765/1/45

THE THOMSON SURFACE. III. TRACKING FEATURES IN 3D

T. A. Howard[1], S. J. Tappin[2], D. Odstrcil[3,4], and C. E. DeForest[1]
[1] Southwest Research Institute, 1050 Walnut Street, Suite 300, Boulder, CO 80302, USA; howard@boulder.swri.edu
[2] National Solar Observatory, Sunspot, NM 88349, USA
[3] George Mason University, 4400 University Drive, Fairfax, VA 22030
[4] NASA/GSFC, Mail Code 674, Greenbelt, MD 20771, USA
Received 2012 August 28; accepted 2012 December 17; published 2013 February 14

ABSTRACT

In this, the final installment in a three-part series on the Thomson surface, we present simulated observations of coronal mass ejections (CMEs) observed by a hypothetical polarizing white light heliospheric imager. Thomson scattering yields a polarization signal that can be exploited to locate observed features in three dimensions relative to the Thomson surface. We consider how the appearance of the CME changes with the direction of trajectory, using simulations of a simple geometrical shape and also of a more realistic CME generated using the ENLIL model. We compare the appearance in both unpolarized B and polarized pB light, and show that there is a quantifiable difference in the measured brightness of a CME between unpolarized and polarized observations. We demonstrate a technique for using this difference to extract the three-dimensional (3D) trajectory of large objects such as CMEs. We conclude with a discussion on how a polarizing heliospheric imager could be used to extract 3D trajectory information about CMEs or other observed features.

Key words: methods: data analysis – solar–terrestrial relations – Sun: corona – Sun: coronal mass ejections (CMEs) – Sun: heliosphere

Online-only material: color figures

1. INTRODUCTION

The current generation of heliospheric imagers observe unpolarized light in the sky beyond around 20° from the Sun. Structures observed by heliospheric imagers are made visible by the Thomson scattering of sunlight from the free electrons in the plasma comprising the solar wind. The physics of Thomson scattering (e.g., Schuster 1879; Minnaert 1930; Billings 1966; Howard & Tappin 2009a) governs the appearance of solar wind features in heliospheric images. Thomson-scattered light yields a radiance that depends on electron density, illumination, and scattering angle at each point along each line of sight. The last two effects vary in opposite directions along the line of sight, leading to a broad "Thomson plateau" of equal radiance per unit density over a broad range of exit angles (Howard & DeForest 2012). The Thomson plateau surrounds the "Thomson surface" defined by Vourlidas & Howard (2006), which is the sphere with diameter extending from Sun center to the observer, and comprises the points of closest approach to the Sun of each line of sight. This term, along with its equivalent "Thomson sphere" are now commonly used in publications involving heliospheric image analysis (e.g., Lugaz et al. 2008; Howard & Tappin 2009a; Sheeley & Rouillard 2010; Möstl et al. 2010). In Paper I of this series (Howard & DeForest 2012), we demonstrated that the TS has no particular significance to instrument sensitivity or to mass calculation involving unpolarized heliospheric imaging, other than denoting the center of the broad Thomson plateau.

In Paper II of this series (DeForest et al. 2013), we showed that when one observes polarized Thomson-scattered light at large elongations from the Sun (as opposed to the unpolarized white light measurements available in the current generation of heliospheric imagers), the TS becomes much more significant. This is because the polarized Thomson-scattering efficiency is maximized on the TS (while it is minimized there for unpolarized light), as are the density and incident light. This effect has been noted and used extensively in coronagraphs (e.g., Poland & Munro 1976; Crifo et al. 1983; Moran et al. 2010; de Koning & Pizzo 2011), and was noted by Howard & Tappin (2009a) in the heliospheric imager context. This suggests that the differences between unpolarized ($B \equiv B_T + B_R$) and polarized ($pB \equiv B_T - B_R$) heliospheric images can be used to directly obtain information about the observed features (B_T and B_R are the tangential and radial components of the scattered radiance and pB is the excess polarized radiance). This ability therefore represents a potentially powerful tool in the analysis of solar wind transients such as coronal mass ejections (CMEs), corotating interaction regions (CIRs), and smaller transient phenomena such as solar wind blobs (Sheeley et al. 2009) and disconnection events (e.g., DeForest et al. 2012).

In this, the third and final installment in our series on the TS, we consider the problem of locating CMEs in three dimensions using the polarization signal and the theory presented in Papers I and II. No polarizing heliospheric imager has yet been constructed, and so we must rely on simulated heliospheric images of CMEs. We consider two simulations:

1. a simple symmetric CME superimposed onto a homogeneous solar wind, and
2. a more realistic CME embedded in MHD solar wind produced using the ENLIL model;

and examine the changes in the unpolarized and polarized radiance of the CME as its trajectory relative to the observer (and therefore the TS) changes. We find that the unpolarized appearance changes little even when the CME is on the far side of the Sun, while its polarized appearance changes at a much more rapid rate, almost disappearing for a far-sided CME. We show that a comparison of the two components enables the extraction of accurate three-dimensional (3D) location and density information using even very crude strawman models of the structure to inform the 3D analysis. We conclude with a discussion on analysis techniques that may be employed using a future polarizing heliospheric imager.

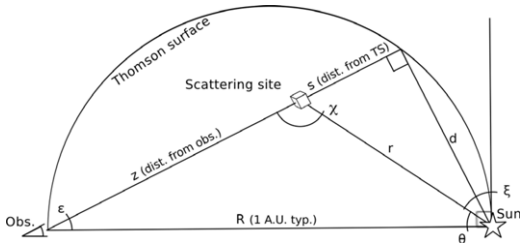

Figure 1. Geometry of a small volume Thomson-scattering light from the Sun, with the locations of the observer (Obs.), the Thomson surface, and relevant angles shown. Reproduced from Figure 4 of Paper I and Figure 1 of Paper II.

1.1. The Thomson Surface Series: A Brief Recap

To reintroduce some relevant quantities, we here recap Papers I and II. There we showed that the radiance B can be represented as the product of three separate functions:

$$dB = k_{\rm TS}(\varepsilon)G(\chi)n_e(s, \varepsilon, \xi)ds, \quad (1)$$

where n_e is the electron number density in the scattering volume, s is the distance along the LOS through the scattering volume, measured relative to the point of closest approach to the Sun along the LOS (i.e., the TS), and ξ is the angle of the scattering volume from the plane of the sky (hereafter referred to as the sky angle). Figure 1 shows the geometry of the setup (also Figure 4 of Paper I and Figure 1 in Paper II). The functions $k_{\rm TS}$ and G depend only on the solar elongation angle ε and the scattering angle χ, respectively, and the G function includes all χ dependence in the (ε, χ) formulation. This determines the rate at which the radiance falls off with distance from the TS. In unpolarized light,

$$G = 1 - \cos^4 \chi. \quad (2)$$

In Paper II, we showed that in excess polarized light, while $k_{\rm TS}$ and n_e in Equation (1) remain the same, the G function becomes

$$G_P = \sin^4 \chi. \quad (3)$$

The difference between G and G_P has important implications for the appearance of features measured by a heliospheric imager. The G function has a very broad peak centered on the TS due to the fact that it superosculates the function $f(\chi) = 1$ there, while the G_P peak is much narrower. This implies that features observed in unpolarized scattered light will be detectable at large distances from the TS (this was validated using observations by the *STEREO*/HIs in Paper I), while their observed radiance should drop off much faster with distance from the TS when observed in pB. Figure 2 shows the variance of unpolarized B and polarized pB radiance per unit surface density of material, as a function of the sky angle ξ.

In Paper II, we demonstrated that it is possible to determine the locations of small features in three dimensions, by measuring the pB/B ratio across a range of ε. We discussed the full scattering theory with appropriate simplifications, including: closed form inversion of the pB/B ratio to determine location; a survey of the effect of the signal-to-noise ratio (S/N) on the determination of the 3D geometry of small features; and limited forward modeling of selected feature types to show that the effect is present also on distributed features.

2. SIMULATIONS OF HELIOSPHERIC IMAGES OF CMES

Application of the theory of Thomson scattering to heliospheric imagers is discussed by Vourlidas & Howard (2006), Howard & Tappin (2009a), Howard (2011), and most recently by Xiong et al. (2012) and our Papers I and II (Howard & DeForest 2012; DeForest et al. 2013). Xiong et al. (2012) performed an MHD simulation on an interplanetary shock and considered changes in the appearance in a heliospheric imager observing both unpolarized and polarized light. Papers I and II included the effects of background noise and also discussed the crucial difference between radiance and intensity when interpreting heliospheric images. Paper II covered the analytic theory of pB detection and small feature location and provided simulated results of the radiance and intensity response for three simple structures in the heliosphere: a small transient, a large CME, and a CIR. We now extend this analysis to include a more realistic simulated CME and empirical 3D location of it, expanding on Paper II's demonstration of polarization effects.

2.1. The Simple Approach (TH)

The simple picture is provided by a crude model developed for the purposes of providing simulated leading edges for the TH Model (Tappin & Howard 2009). This approach is slightly more sophisticated than the first-cut model in Paper II. A homogeneous background solar wind is produced via the following function:

$$n_e \sim \begin{cases} R^{-2.45}, & R \leqslant 1.0\,\text{AU} \\ R^{-2}, & R > 1.0\,\text{AU} \end{cases}, \quad (4)$$

where R is the distance from the Sun, with boundary condition $n_e(R = 1.0\,\text{AU}) = 5\,\text{cm}^{-3}$; these values were obtained by fitting to the tabulated values in Allen (1973). The CME is introduced as a simple $\times 2$ multiplier of the solar wind density,

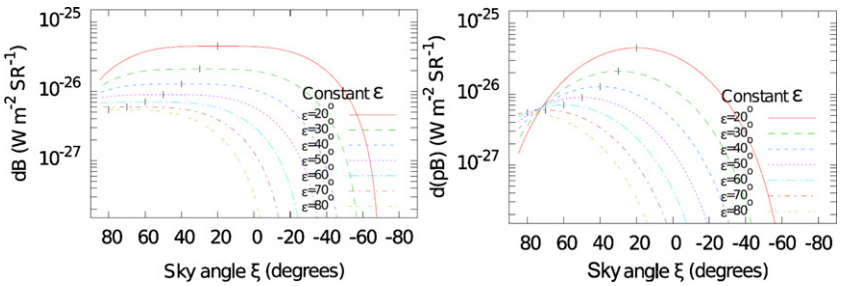

Figure 2. Scattered radiance observed in unpolarized (dB, left, from Figure 5 of Paper I) and polarized ($d(pB)$, right, from Figure 3 of Paper II) white light scattered from a unit path length of plasma at different locations along different lines of sight (i.e., constant elongation ε). These are plotted as a function of the angle from the sky plane (the sky angle ξ). The location of the TS is indicated with the black vertical bars. Note that dB drops off at a much more gradual rate than $d(pB)$ as the unit path length of plasma moves away from the TS.

(A color version of this figure is available in the online journal.)

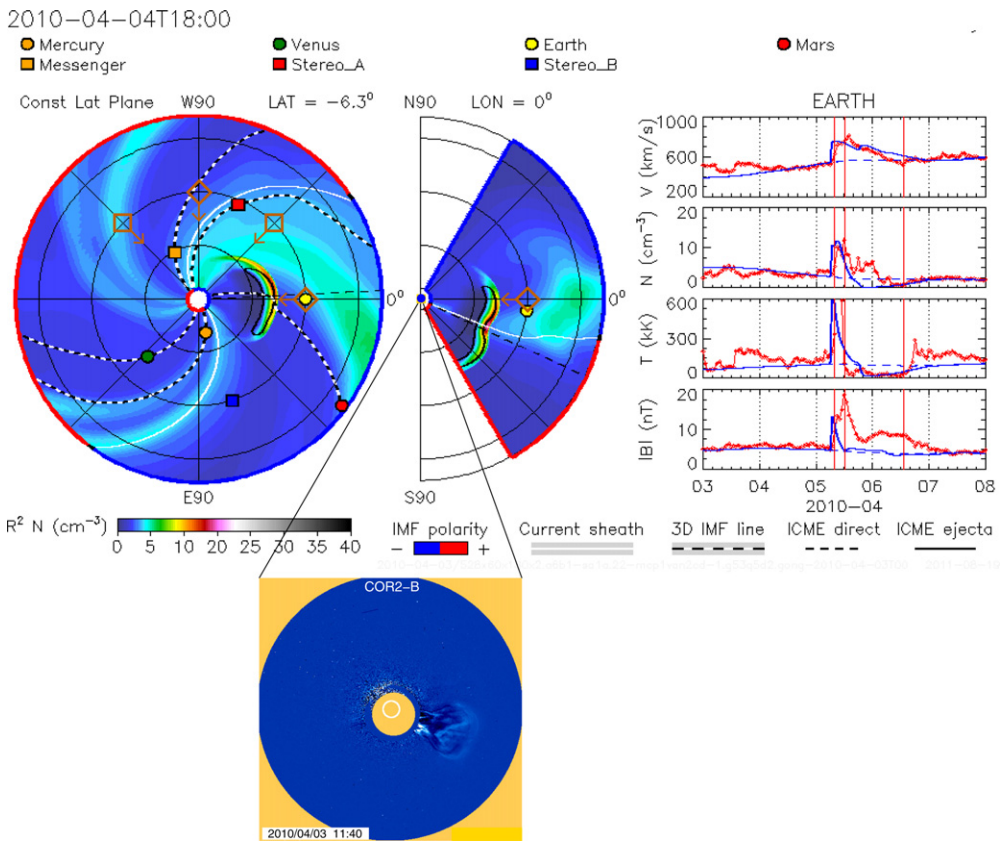

Figure 3. ENLIL model reconstruction of the Earth-directed CME first observed on 2010 April 3. Left: constant latitude plane (containing the Earth) slice (looking down from the north) onto the solar wind out to a distance of 1.2 AU from the Sun. Density normalized by r^2/R is indicated with the color scale, along with the locations of various spacecraft and planets. The CME is the high-density feature with the black outline moving toward the Earth. This shows the CME in its original modeled orientation: shown here at its location on April 4 at 18 UT. Middle: the same image with a solar meridional (north–south) slice, showing the CME somewhat to the south of both the solar equator and the ecliptic plane. A COR2-B image from April 3 at 1139 UT is included as an inset, showing the CME as it appeared when it was close to the Sun. The brown diamonds indicate the locations of the observer when synthetic images were determined multiple times: Arrows indicate that their fields of view are centered on the Sun. Right: simulated (blue) and actual (red) *ACE* density measurements at the Earth for the time period from April 3–8.

(A color version of this figure is available in the online journal.)

with its structure as a symmetric spherical arc of total latitude and longitude width of 60° and a radial thickness of 0.1 AU. The method of computing the maps of such CMEs is described in more detail in Tappin & Howard (2009).

2.2. The Sophisticated Approach (ENLIL)

We used the ENLIL code (Odstrcil et al. 2004, 2005) to simulate a CME under conditions more realistic than the simple approach discussed in the Section 2.1. ENLIL models the background solar wind (density and magnetic field) via synoptic maps of the radial velocity and magnetic field, derived using the Wang–Sheeley–Arge (WSA) model for photospheric magnetogram data sets (Arge & Pizzo 2000; Arge et al. 2003), and injects the CME as a volume of increased density. The shape of the volume is governed by coronagraph measurements, with the former determined by the CME cone model (Zhao et al. 2002; Xie et al. 2004), and the latter by empirical brightness measurements of the CME to be simulated. We have selected a simple real CME for our study: the geoffective one that erupted from the Sun on 2010 April 3 and reported by (among others) Möstl et al. (2010), Wood et al. (2011), Rouillard et al. (2011), and Temmer et al. (2011). The original simulated CME was centered at S25W03, had a half-width of 37°, an initial speed of 960 km s^{-1} and an initial density 4× that of the fast solar wind stream value. This was modeled as a spherical homogeneous structure. This is shown in its original orientation in Figure 3. We changed the location of the observer by rotating the ENLIL output grid about the polar axis; note that for the purposes of this study we have placed the observers at the notional solar equator rather than the ecliptic for computational convenience. We used rotations of 0°, 45°E, 90°E, and 135°E such that the location of the simulated CME relative to the observer was comparable to that from the simple model. We then generated forward-modeled maps of B, pB, and pB/B in the same manner as for the simple simulation (Odstrcil & Pizzo 2009).

2.3. Simulation Protocol

In both approaches we modeled the same CME propagating in four different directions, such that its central axis originated in the solar-equatorial plane along four radial vectors. For the simple CME the propagation was directly toward the observer ($\xi = 90°$) and along the $\xi = [+45, 0, -45]°$ vectors. For the ENLIL simulation, the original Sun–Earth line was transformed to those same vectors, the central axis of the CME at injection being 25°S and 3°W of that. For consistency we refer to these as the $\xi = 90°$ case, etc. For each trajectory we produced a zenithal equidistant ("fisheye") map for B, pB and the ratio pB/B. (Fisheye maps were commonly used with the SMEI heliospheric imager (Eyles et al. 2003; Jackson et al. 2004) and have the useful properties that the Sun is at the center of the map and elongation contours are perfect circles with uniform spacing.) We then subtracted the background solar wind from

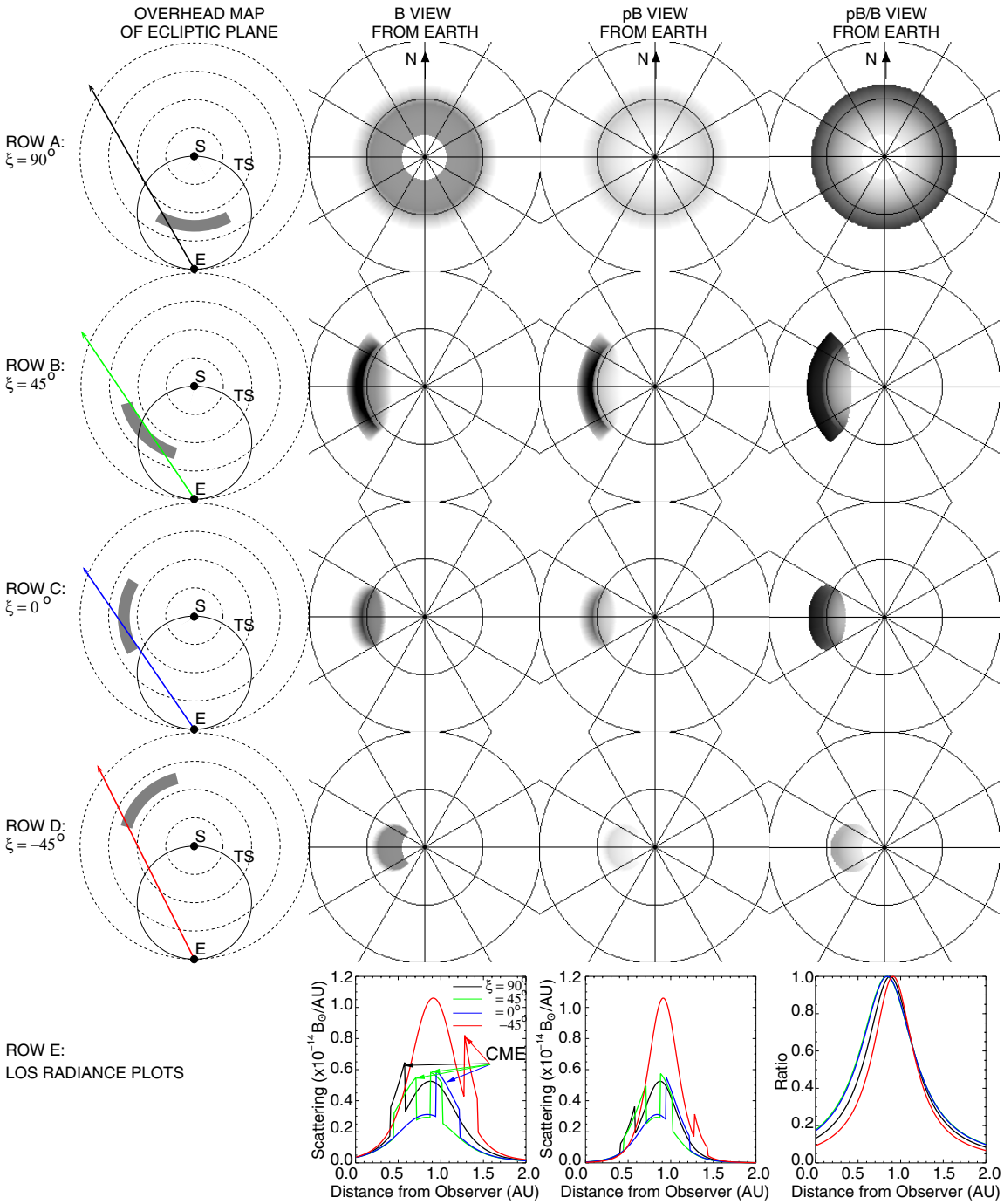

Figure 4. Results from the simple CME simulation in a homogeneous solar wind described in Section 2.1. The left column shows the ecliptic plane slice of the location of the CME at which the maps were produced. The Sun S and observer (assumed to be the Earth) E are shown along with dashed 0.2 AU contours. In each case the line of sight is selected such that it passes through the location of the CME where its apparent radiance is largest. The plots of radiance vs. distance from observer along each line of sight, color-coded to match the color on the left column, are shown along the bottom row. The second, third, and fourth columns show background-subtracted fisheye maps of each CME as observed in B (second column), pB (third), and pB/B (fourth). Each map is normalized to the same radiance range: 0–10^{-15} $B_\odot$ for the B and pB maps; 0–1 $B_\odot$ for pB/B. The Sun is at the center of the map and each contour (radial line) indicates 30° elongation (position angle).

(A color version of this figure is available in the online journal.)

the fisheye maps based on image analysis (blind to the model), to reveal only the projected CME.

2.4. Simulation Results and Demonstration Images

Figure 4 shows the simulated images of the simple CME at the same distance from the Sun (0.5 AU) along each of the four trajectories. The top row shows an idealized version of the familiar halo CME centered on the 30° elongation contour as expected for an Earth-directed transient at a distance of 0.5 AU. As shown in the ecliptic plane slice on the left, this CME is some distance from the TS, and the pB map is clearly much fainter than the B map. The radiance scales are identical, with full black representing 10^{-15} $B_\odot$ and white representing 0. The pB/B view is scaled 0–1, with 0 being white and 1 black.

The B and pB maps are very similar for the $\xi = 45°$ case, since this CME intersects the TS. The $\xi = -45°$ CME is almost

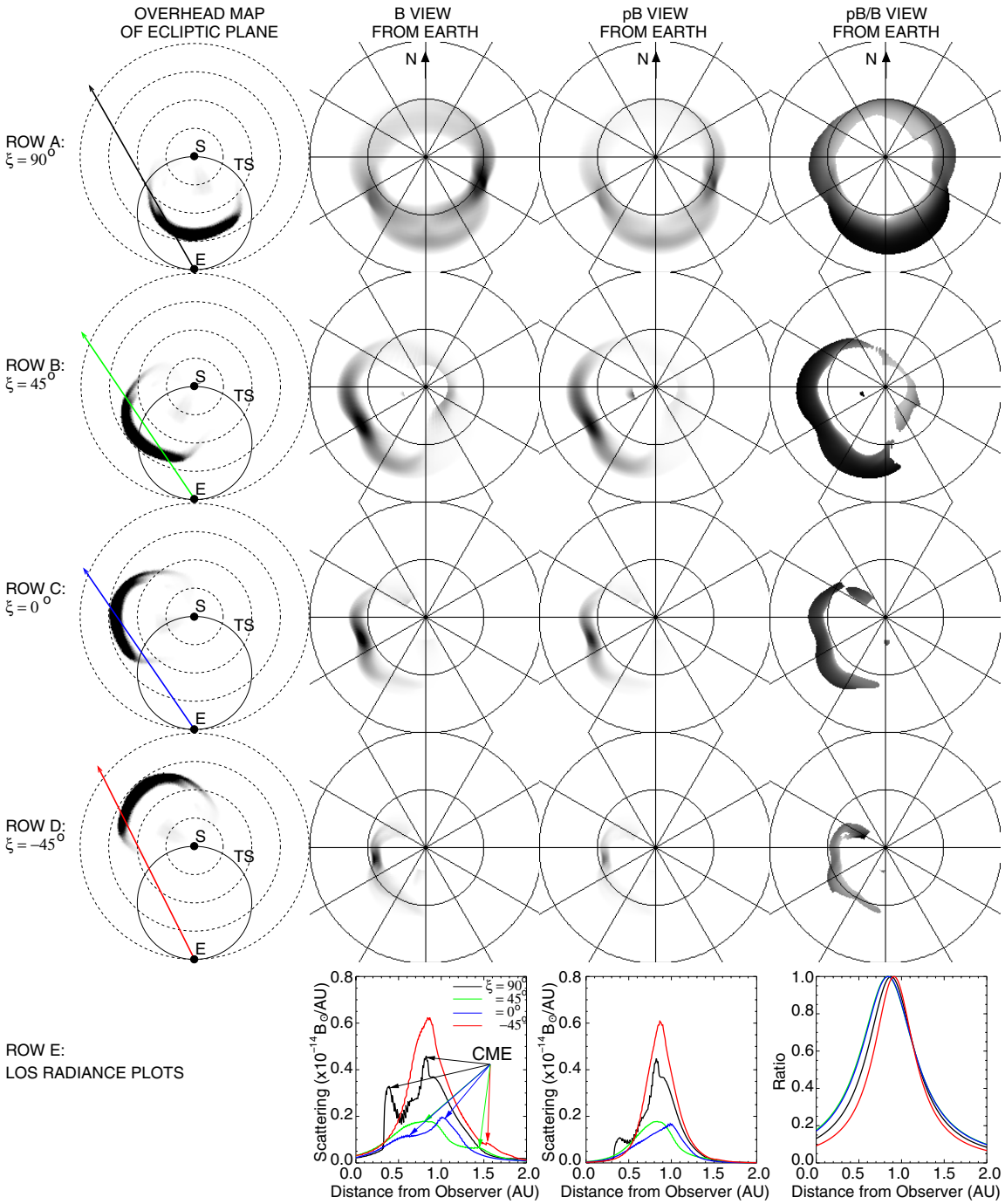

Figure 5. Results from the ENLIL CME simulation in the modeled MHD solar wind described in Section 2.2. The solar wind and CME conditions were chosen for the period from early 2010 April, when a large geo-effective CME erupted from the Sun. While the parameters of the CME are the same as that event (centered at S25W03; initial speed 960 km s^{-1}; initial density 4× that of the fast solar wind stream), its trajectory has been artificially altered such that its central vector is the same as that for the simple simulation. The display is identical to that shown in Figure 4 with the ecliptic projection in the first column, selected lines of sight such that they pass through the brightest point, and the background-subtracted fisheye maps for B, pB, and pB/B. The scale is also the same for each map.

(A color version of this figure is available in the online journal.)

invisible in pB since it is some distance from the TS, but it is still quite visible in B. These simulations show that, with a simple CME in a homogeneous solar wind, the variations between B and pB are significant and measurable as we move the CME away from the TS, as demonstrated in Paper II.

Figure 5 shows the same display as for Figure 4, for the more realistic CME simulated using ENLIL. In this case, the pB/B images have been truncated where the total brightness is below $3 \times 10^{-17}\ B_{\odot}$. As with Figure 4, the multiple peaks across the bottom row indicate both the solar wind and double crossings of the LOS through the CME for all but the $\xi = -45^{\circ}$ case. The CME crossings are indicated with arrows. Note that the CME peaks that are a large distance from the TS are significantly reduced in pB, and the width of the peak for the $\xi = 45^{\circ}$ case is smaller in pB. The observed brightness of the CME is significantly reduced in the fisheye pB maps compared with B, just as was the case for the simple CME in Figure 4.

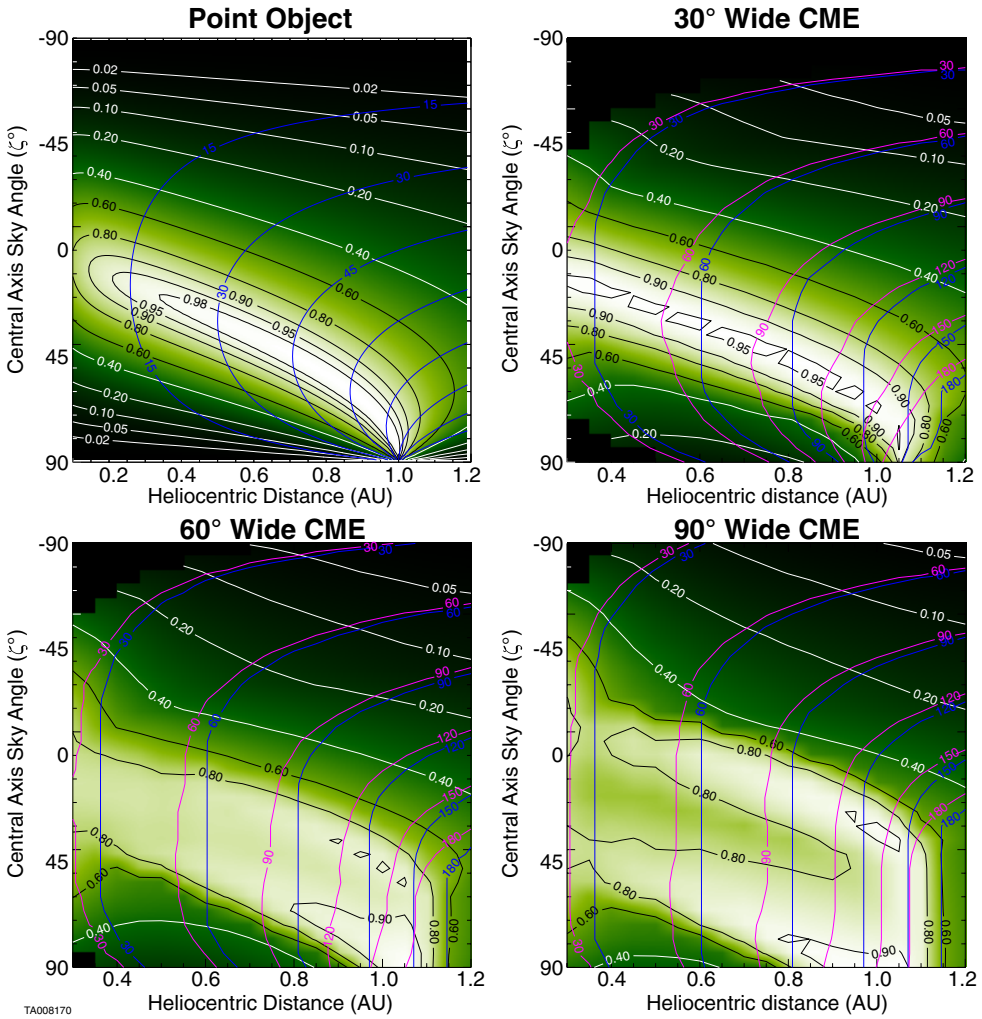

Figure 6. Plots of pB/B (color-coded; black and white contours) with sky angle ξ (y-axis) and distance R from the Sun (x-axis), for transient structures of varying sizes. The elongation angles (in degrees) are represented by the blue contours. The top left plot shows the small packet case, and the other plots are for basic-simulation spherical-shell CMEs with total latitude/longitude widths of 30° (top right), 60° (bottom left), and 90° (bottom right). Additional magenta elongation contours are provided for the CME cases, which represent the half maximum value of B ahead of the CME (i.e., the approximate location of the leading edge). The blue contours show the elongation of the maximum B. As with the small volume element case, a polarizing heliospheric imager provides pB/B and ε measurements (for the CME case the observer also needs to identify whether they are measuring the leading edge of maximum value—i.e., blue or magenta ε contour), and the cross-over points of the two contours provide axis values of ξ and R.

(A color version of this figure is available in the online journal.)

The background-subtracted fisheye maps reveal a similar tendency to that observed in the simple case: the difference in appearance between B and pB increases significantly with increasing distance from the TS.

3. THREE-DIMENSIONAL SIGNAL AND INVERSION

Paper II describes the means by which we can use pB (via the pB/B ratio) to determine the 3D location of a small feature and the inherent level of precision in such measurements. However, large structures such as CMEs have more complex variations of pB/B than do idealized small features. Because of this, the simple analytical inversion is no longer possible and an alternative approach must be developed. In this section, we describe a technique to identify the 3D location of large features such as CMEs observed with a heliospheric imager capable of performing both B and pB observations. We briefly recap and expand on the Paper II results for small features and build the forward model discussed in Section 2.1 into a method for inverting CME propagation via parametric fitting. Our method is based on the TH model (Tappin & Howard 2009) for CME trajectory extraction, but makes use of pB effects rather than perspective effects to extract 3D trajectory.

Paper II demonstrated how the pB/B ratio can be used to identify the location of a small feature in 3D space. For any elongation ε, a pB/B versus ξ plot produces a distinct curve, from which ξ can be determined with measured values of pB/B and ε. In the small feature case, the expression can be inverted analytically (see Equation (12) and Figure 7 of Paper II).

When the feature is observed by a polarizing heliospheric imager, measurements of pB/B and ε are obtained directly from the images. Figure 6 shows pB/B measurements across a continuum of trajectories and elongations for transients of varying size, from a small volume element (top left), to a CME with a total angular width of 90°. For the finite-sized CMEs, the values of pB/B are averaged over the whole area of the CME in the map. The CMEs are assumed to be of the same structure as in the simple approach (Section 2.1), i.e., as a solar-centric spherical cone with equal latitudinal and longitudinal width. We regard this as a prototype polarizing equivalent of the

Table 1
Summary of the Fitting Results from pB/B and the TH Model for the ENLIL CME in Different Orientations

Input ξ (°)		Fitted ξ (°)		Fitted Speed (km s^{-1})		Fitted Launch (2010 Apr)	
Nominal	True	pB/B	TH	pB/B	TH	pB/B	TH
90	65	67 ± 10	73 ± 4	712	725	3 00:40	3 00:30
45	42	36 ± 7	37 ± 5	1048	790	3 11:50	3 03:20
0	3	10 ± 7	10 ± 40	586	900	2 19:10	3 04:50
−45	−37	-13 ± 7	-34 ± 7	445	1000	2 16:30	3 12:00

Note. For comparison, the initial CME speed provided as a boundary condition in the ENLIL simulation is 960 km s^{-1} (Section 2.2).

TH model with fewer variable parameters than are possible or desirable for a production system, in order to demonstrate this type of inversion.

In the small volume element case (top left panel of Figure 6) the elongation ε values are the blue contours. The 3D location (ξ, R) can be identified using measurements of pB/B and ε, where the crossover between the two contours leads to the (ξ, R) values. As is clearly shown, for the single volume case there are two (ξ, R) values that arise from a single (pB/B, ε) measurement. This is demonstrated for two values of ξ in Figures 5 and 6 of Paper II. The correct values of ξ and R can be identified with a sequence of pB/B and ε measurements: one group of points will produce values that cluster around a single value of ξ, while the other will produce values with a larger variance. The latter describes the "ghost" trajectory discussed in Paper II, which arises from the symmetric nature of G_P: the group of points at the same distance from the TS but in the direction opposite to where the true trajectory points. The top left panel of Figure 6 shows that for multiple measurements of a small packet moving through the heliosphere, the values of ξ and R (i.e., location in 3D space) can be accurately determined solely from pB/B and ε measurements.

The situation becomes more complicated as the size of the CME increases. The remaining panels in Figure 6 show the pB/B continuum for simple-model CMEs of selected increasing sizes. Here there are two groups of ε contours corresponding to the maximum B (blue) and half of the maximum B (magenta), which we use as an approximation to the location of the leading edge. Consider, for example, the 90° wide CME in the bottom right panel of Figure 6. Its continuum has two pB/B peaks arising from the dense, hollow shell of the CME crossing the TS twice, with each peak being where one of the crossings is close to the Thomson surface. Here one can obtain four (ξ, R) values from a single (pB/B, ε), corresponding to the true trajectory and three ghost trajectories. As with the small packet case, however, a single trajectory can be identified with multiple measurements by extracting the group of points with the smallest variance as the CME propagates. Figure 7 shows plots of the evolution of pB/B averaged over the whole CME as it propagates out from the Sun, versus R and ε for a selection of ξ values (horizontal slices through Figure 6).

3.1. Application to an Example Event

To clarify the interpretation of Figures 6 and 7, we present an example event and present a procedure for determining its exit angle from observed geometry and the pB/B signal, in a similar manner to how the TH model is used with unpolarized measurements. This procedure is performed on the simulated example event presented above (early 2010 April).

The first step is to apply the crude assumption that the CME has the form of a perfect spherical shell. The width of the shell is assigned from the width of the CME, estimated using measurements of the position angle (PA) width from coronagraph images. (In a production model using only Earth-based images, halo CME extent would be derived through a combination of pB/B and feature shape evolution, augmenting the current shape-based method used by the TH model for unpolarized heliospheric images.) A COR2-B image of the example CME is shown as an inset in Figure 3. The PA width of the CME, measured using both COR2-A and COR2-B, is approximately 60°. Its ($\xi - R$) versus ($pB/B - \varepsilon$) contour plot can therefore be approximated by that shown in the bottom left panel of Figure 6. We made (pB/B, ε) measurements of five images generated from the ENLIL densities from this event, at times of [06,12,18] UT on April 4 and [00,06] UT on April 5. The elongation measurements were made at PA of 90° (i.e., directly to the left) for all but the $\xi = 90°$ case, where measurements were made at PA = 180° (directly down). This location was chosen as it approximated the maximum brightness location of the CME in each image. As with the pB/B maps in Figure 6, the value of pB/B is an average over the whole CME—which we consider to be the region where the excess brightness is greater than 3×10^{-17} $B_\odot$. Each measurement group was assigned to the contour plot.

The results for the CME directed in the four different directions are shown in Figure 8 and summarized in Table 1. In all but the $\xi = 45°$ (blue) case there are two groups of points. These represent the true and "ghost" trajectories predicted in Paper II. The branch with the smallest variance (σ^2) corresponds to the true trajectory in all but the −45° case. Note that the $\xi = 45°$ breaks off into four branches at around 0.7 AU from the Sun. The reason for this is that the LOS passes through the dense part of the CME in two locations when it reaches this distance from the Sun, and each of these intersections produces a maximum of pB/B when it is close to the Thomson surface, leading to one true and three ghost trajectories.

As a point of reference, we also fitted the geometry and speed of the CME using the TH model (Tappin & Howard 2009). This was done by taking the maps generated from the ENLIL densities and measuring the leading edge manually just as we have done for real CME observations from SMEI (see, e.g., Howard et al. 2006, 2007; Tappin & Howard 2009; Howard & Tappin 2009b, 2010). These measured leading edges were then processed using the TH fitting programs exactly as if they were measurements from real SMEI data.

In Figure 8, the true sky angles (the central axis of the original CME injection) are indicated by horizontal solid lines, the sky angles determined from pB/B are shown by horizontal dashed lines, and the TH determinations by horizontal dotted lines.

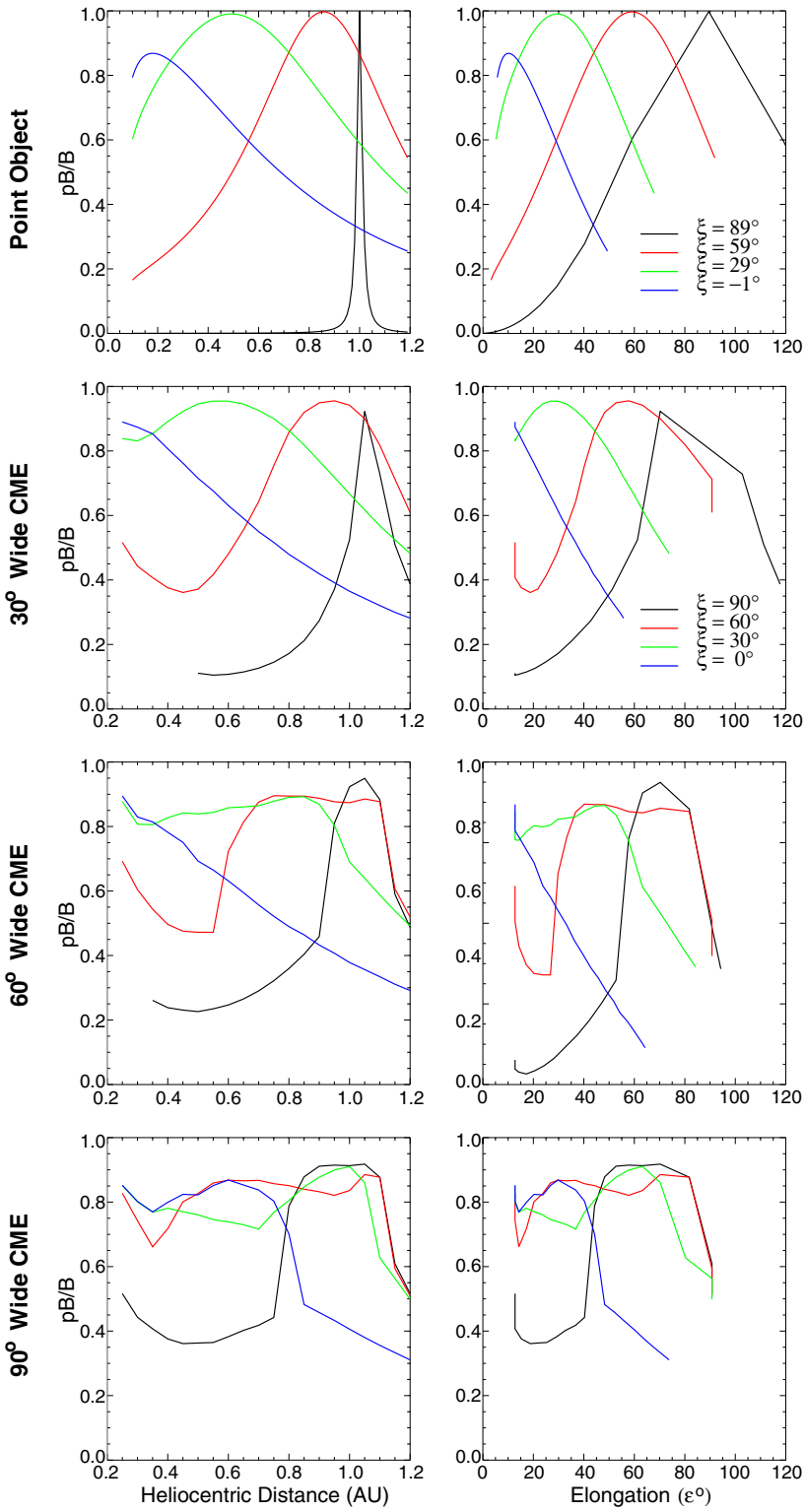

Figure 7. Plots of the evolution of pB/B vs. R (left) and ε (right) as the CME travels out from the Sun, for each of the cases plotted in Figure 6. Each color represents a single ξ (horizontal) slice through the Figure 6 plots.

(A color version of this figure is available in the online journal.)

For the three cases where the CME is centered in front of the sky plane, the direction inferred from pB/B is within 1σ of the input value. For the far-sided case, there is a greater discrepancy (about 3.5σ); this case is discussed in more detail below.

By comparison, the TH fits show a very similar performance for the $\xi = 45^\circ$ case, while pB/B is slightly better for the $\xi = 90^\circ$ case and TH is somewhat better when $\xi = -45^\circ$. For the case where $\xi = 0^\circ$, although the actual values are very similar, the uncertainty in the TH fit is very large while that from pB/B is similar to those in the other directions. We interpret this as meaning that near the sky plane there exists a wide region of directions within which the geometry of the

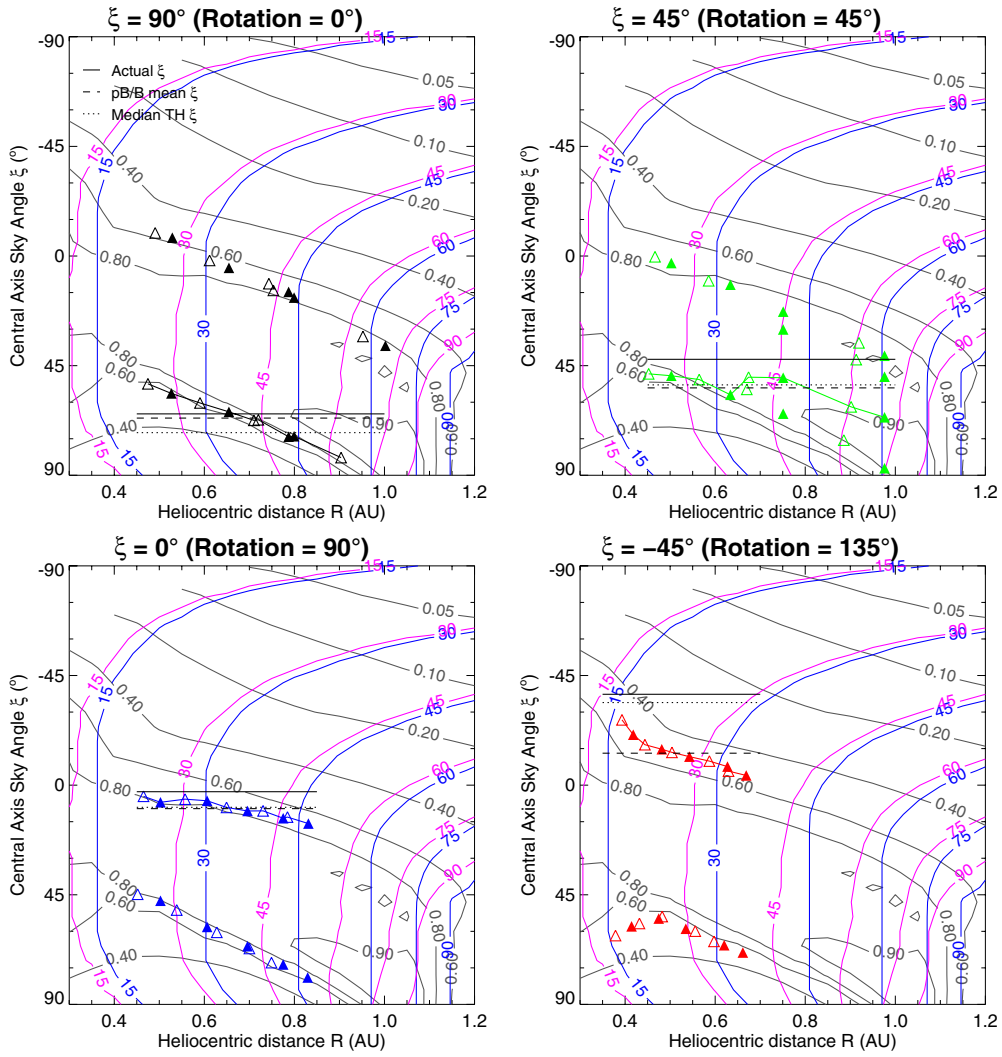

Figure 8. Contour plots of pB/B and ε for the 60° width CME used to determine the height and direction of the simulated ENLIL CME, with measurements of pB/B and ε assigned. Measurements were made for five ENLIL images, at times 06, 12, and 18 UT on 2010 April 4, and 00 and 06 UT on April 5. Values are shown for the CME directed in the four directions shown in Figure 5: (top left) the $\xi = 90°$ case; (top right) the $\xi = 45°$ case; (bottom left) $\xi = 0°$; (bottom right) $\xi = -45°$. The actual ξ accommodates for the fact that the simulated CME was directed somewhat southward of the ecliptic plane and is shown as a solid horizontal line in each case. Each ENLIL image results in two points: one for the maximum B (solid triangle) and one for the leading edge (open triangle). The group of points with the smallest variance (σ^2) has been assigned a curve through it and the mean of each pB/B group is indicated with the horizontal dashed line. The direction ξ of the CME can be estimated using this mean value, and the varying heliocentric distance (R) can be measured from the x-axis readings at this ξ. For comparison with existing techniques with unpolarized heliospheric imagers, the value of ξ from the TH model for the same event is shown in each case as a horizontal dotted line. This is the median value of ten TH model runs on the simulated CME.

(A color version of this figure is available in the online journal.)

leading edge changes little. Thus we can conclude that even in its present primitive form, direction determination using pB/B exceeds the performance of the TH model for CMEs in the near-side hemisphere, as it substantially reduces the uncertainty in direction for those cases where the leading edge is consistent with a wide range of different geometries.

With a value of ξ established, we may now extract the R values for each time, simply by reading them off from the x-axes of Figure 8 at the determined value of ξ (the dashed horizontal lines). We can then evaluate the performance of this version of the pB/B technique on reproducing a kinematic profile of the simulated CME. Distance–time plots for the leading edge measurements in each case are shown in Figure 9. For reference, we have included the following: (1) distance–time information for the associated (real) CME observed by COR2-A (the orange crosses), (2) the time of the arrival of an associated (real) forward shock near Earth, measured by the *ACE* spacecraft (magenta circle), and (3) the constant speed solution of the TH model for the (simulated) CME in each case (dotted lines). The most accurate pB/B result is for the $\xi = 90°$ case, which performs slightly better than its TH counterpart, with the accuracy of the reconstruction declining as the central axis of the CME moves further from the Sun–observer line. The speeds computed by fitting a straight line to the pB/B points and those from the TH fits along with the inferred launch time of the CME are included in Table 1.

The pB/B method performs significantly worse than TH for the $-45°$ case, which bears examination. First, the group of points with the largest variance is in fact the lower branch, which, if selected, would indicate that the CME was closer to 60° ahead of the sky plane rather than its true value of 37° behind the sky plane. TH predicted the location of the CME well in this case, still better than the pB/B technique even when the upper branch was selected (pB/B produced a mean $\pm\sigma\xi$ of

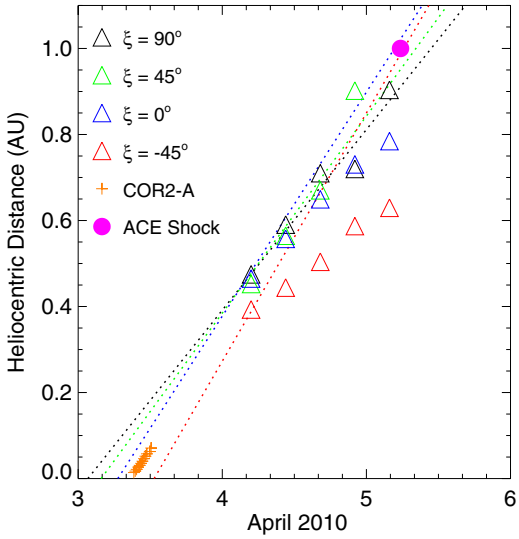

Figure 9. Distance R vs. time plots for each of the four simulated cases shown in Figure 8, with the same colors and symbols for each case. For reference, distance–time plots measured from COR2-A images of this CME are included, as is the timing of the arrival of a forward shock associated with this event at the *ACE* spacecraft. The TH speed results have been extended such that they cover the entire distance range.

(A color version of this figure is available in the online journal.)

$-13 \pm 7^\circ$). This result is less than 20° from the actual value of ξ, but in this case it was better to remain with the unpolarized TH model results. However, it should be kept in mind that the pB/B fitting made no use of the timing information that would be used in any operational code, and the slowing of the CME's apparent movement across the sky is crucial to showing that it is far-sided. Also in this case the pB image is very faint, and so the uncertainties of exactly where to cut off the edge of the CME for the pB/B determination could make a significant difference in the value of pB/B obtained.

In summary, we find that even in its current form the use of pB/B gives directions of improved accuracy (i.e., comparable values with reduced uncertainty) to the TH model for near-sided CMEs. It is also clear that when it is possible to combine both pB/B and geometrical information we should be able to obtain well-constrained and accurate determinations of CME kinematics for most if not all CMEs.

4. DISCUSSION

The results from the two simulations confirm the theoretical results given in Papers I and II: that the distance of the CME from the Thomson surface plays little role in feature appearance when observing at large angles from the Sun in unpolarized light, and that it plays a significant role when observing polarized light. These differences can be used to determine the 3D location of a feature. When observing unpolarized light, the presence of the Thomson plateau (Paper I) renders the notion of the Thomson surface unimportant for most feature trajectories, reducing the problem of 3D analysis of these features simply to geometry and density.

In other words, the ability to neglect the TS when observing in unpolarized light enables the accurate calculation of the density of a feature (see Figure 8 of Paper I), and the significance of the TS in polarized light enables the calculation of the 3D location of the feature (see Figure 7 of Paper II). These measurements can be made by a heliospheric imager acting alone with no auxiliary measurements or from distant viewpoints. We have demonstrated a simple forward-modeling based technique for tracking CMEs through the heliosphere using only a combination of polarized and unpolarized heliospheric images. Despite its crudeness this technique exceeds the performance of an existing well-characterized tool for near-sided CMEs, as it substantially improved the constraints in the cases where geometrical considerations alone allowed a wide range of possible reconstructions. From the success of this proof of concept analysis, we conclude that it is possible to exceed the performance of a side-viewing, distantly located heliospheric observatory for space-weather tracking, with a single, near-Earth instrument capable of quantitative polarized imaging. A future CME tracking system could include a polarizing heliospheric imager and a more sophisticated inversion tool than the pB/B proof-of-concept tool developed here. That analysis should include a larger range of parameter degrees of freedom, in a similar parameter space to that used by the existing TH model (latitude, longitude, latitude/longitude width, distortion).

The ability to locate objects both large (CMEs) and small (substructure or boli of solar wind) is dependent on two conditions: the asymmetry with respect to the sky plane of the Thomson surface, which eliminates ambiguity about the exit angle (Paper II); and the ability to extract quantitative photometry of the faint Thomson-scattered signal, which has only recently been developed (DeForest et al. 2011). Now that these two conditions are realized and understood, it is possible to exploit a polarizing heliospheric imager to measure the 3D location not only of small packets of solar wind but also of large, space-weather-relevant events such as CMEs. Such an instrument, properly designed, should be able to achieve better location of bright features than can currently be achieved through unpolarized multi-viewpoint tracking and stereoscopy.

5. CONCLUDING REMARKS

In this three-part series of papers, we have explored the nature of the construction surface dubbed the Thomson surface for unpolarized and polarized heliospheric imaging. We have demonstrated correct technique for multiple applications of quantitative heliospheric imaging, including remote mass determination and remote feature location in three dimensions. The theory of Thomson scattering is well known and has been amplified and/or used by many authors, particularly for understanding narrow-field coronagraph measurements. Now that photometric wide-field Thomson imaging of solar wind features has been realized, we anticipate that the present trilogy will prove to be a useful resource for understanding the applications and limits of heliospheric imaging instruments.

In Paper I, we developed an appropriately simplified theory of Thomson scattering for heliospheric imaging; showed how the cancellation between the scattering-efficiency and illumination-function contributions leads to the surprisingly uniform textural appearance of solar wind in heliospheric imaging data; introduced the phrase "Thomson plateau" to describe the broad range of angles in which the cancellation is a valid approximation; discussed why existing heliospheric imagers are sensitive to CMEs and solar wind features over a broader range of angles than anticipated; and showed how to calculate the mass of a feature given its location in 3D space and intensity in a heliospheric image. In Paper II, we developed an equally simplified theory of heliospheric imaging applicable to a polarizing instrument; discussed applications of polarized heliospheric imaging including reduction of the fixed background and location of features in

3D space; demonstrated that in wide-field images the front/back asymmetry of the Thomson surface overcomes the well-known ambiguity of pB/B positional measurements from narrow-field coronagraph observations; carried out a full analytic analysis for the simplified case of determining the location of small features such as solar wind "blobs;" and demonstrated that large-scale features such as CMEs and CIRs yield measurable position-dependent signal that could be extracted from a pB-versus-B comparison from an ideal instrument. In the present paper, we have explored a specific application of polarized heliospheric imaging: determination of the 3D location and kinematic evolution of propagating CMEs. We conclude that this application is feasible, based on performance of a proof-of-concept forward model using the successful TH model for interpreting CME propagation.

By exploring the nuances of Thomson-scattering physics and how they relate to heliospheric images, we have both demonstrated correct techniques for interpreting those images, and also shown that a next-generation heliospheric imager capable of polarization measurements is a useful next step forward in measuring and understanding interplanetary structures such as CMEs, CIRs, and other solar wind transient phenomena.

Support for this work was provided by an internal grant from the Southwest Research institute and partly by the NSF/SHINE Competition, Award 0849916. S.J.T. is supported at NSO by the USAF under a Memorandum of Agreement. D.O. was partially supported by the AFOSR/MURI project.

REFERENCES

Allen, C. W. 1973, Astrophysical Quantities (3rd ed.; London: Athlone)
Arge, C. N., Odstrcil, D., Pizzo, V. J., & Mayer, L. R. 2003, in AIP Conf. Proc. 679, Proc. 10th Int. Solar Wind Conf. (Melville, NY: AIP), 190
Arge, C. N., & Pizzo, V. J. 2000, JGR, 105, 10465
Billings, D. E. 1966, A Guide to the Solar Corona (San Diego: Academic)
Crifo, F., Picat, J. P., & Cailloux, M. 1983, SoPh, 83, 143
DeForest, C. E., Howard, T. A., & McComas, D. J. 2012, ApJ, 745, 36
DeForest, C. E., Howard, T. A., & Tappin, S. J. 2011, ApJ, 738, 103
DeForest, C. E., Howard, T. A., & Tappin, S. J. 2013, ApJ, 765, 44 (Paper II of this series)
de Koning, C. A., & Pizzo, V. J. 2011, SpWea, 9, S03001
Eyles, C. J., Simnett, G. M., Cooke, M. P., et al. 2003, SoPh, 217, 319
Howard, T. 2011, Coronal Mass Ejections: An Introduction (New York: Springer)
Howard, T. A., & DeForest, C. E. 2012, ApJ, 752, 130
Howard, T. A., Fry, C. D., Johnson, J. C., & Webb, D. F. 2007, ApJ, 667, 610
Howard, T. A., & Tappin, S. J. 2009a, SSRv, 147, 31
Howard, T. A., & Tappin, S. J. 2009b, SSRv, 147, 89
Howard, T. A., & Tappin, S. J. 2010, SpWea, 8, S07004
Howard, T. A., Webb, D. F., Tappin, S. J., Mizuno, D., & Johnson, J. C. 2006, JGR, 111, A04105
Jackson, B. V., Buffington, A., Hick, P. P., et al. 2004, SoPh, 225, 177
Lugaz, N., Vourlidas, A., Roussev, I. I., et al. 2008, ApJL, 684, L111
Minnaert, M. 1930, ZA, 1, 209
Moran, T. G., Davila, J. M., & Thompson, W. T. 2010, ApJ, 712, 453
Möstl, C., Temmer, M., Rollett, T., et al. 2010, GeoRL, 37, L24103
Odstrcil, D., & Pizzo, V. J. 2009, SoPh, 259, 297
Odstrcil, D., Pizzo, V. J., & Arge, C. N. 2005, JGR, 110, A02106
Odstrcil, D., Riley, P., & Zhao, X. P. 2004, JGR, 109, A02116
Poland, A. I., & Munro, R. H. 1976, ApJ, 209, 927
Rouillard, A. P., Odstrcil, D., Sheeley, N. R., et al. 2011, ApJ, 735, 7
Schuster, A. 1879, MNRAS, 40, 35
Sheeley, N. R., Jr., Lee, D. D.-H., Casto, K. P., Wang, Y.-M., & Rich, N. B. 2009, ApJ, 694, 1471
Sheeley, N. R., Jr., & Rouillard, A. P. 2010, ApJ, 715, 300
Tappin, S. J., & Howard, T. A. 2009, SSRv, 147, 55
Temmer, M., Rollett, T., Möstl, C., et al. 2011, ApJ, 743, 101
Vourlidas, A., & Howard, R. A. 2006, ApJ, 642, 1216
Wood, B. E., Wu, C.-C., Howard, R. A., Socker, D. G., & Rouillard, A. P. 2011, ApJ, 729, 70
Xie, H., Ofman, L., & Lawrence, G. 2004, JGR, A03109
Xiong, M., Davies, J. A., Bisi, M. M., et al. 2012, SoPh, in press, doi:10.1007/s11207-012-0047-0
Zhao, X. P., Plunkett, S. P., & Wu, W. 2002, JGR, 107, doi:10.1029/2001JA009143